IVYSPRING INTERNATIONAL PUBLISHER

Theranostics

2020; 10(7): 2965-2981. doi: 10.7150/thno.40858

Review

Using magnetic particle imaging systems to localize and guide magnetic hyperthermia treatment: tracers, hardware, and future medical applications

Prashant Chandrasekharan[1]✉, Zhi Wei Tay[1], Daniel Hensley[2], Xinyi Y Zhou[1], Barry KL Fung[1], Caylin Colson[1], Yao Lu[1], Benjamin D Fellows[1], Quincy Huynh[3], Chinmoy Saayujya[3], Elaine Yu[2], Ryan Orendorff[2], Bo Zheng[1], Patrick Goodwill[2], Carlos Rinaldi[4], and Steven Conolly[1,3]

1. University of California Berkeley, Department of Bioengineering, Berkeley, CA 94720, United States
2. Magnetic Insight, Inc., Alameda, CA 94501, United States
3. Department of Electrical Engineering and Computer Sciences, University of California, Berkeley, CA 94720, United States
4. University of Florida, J. Crayton Pruitt Family Department of Biomedical Engineering and Department of Chemical Engineering, FL, 32611 United States

✉ Corresponding author: E-mail: prashantc@berkeley.edu; Phone: +1 (510) 642 3420

Received: 2019.10.03; Accepted: 2020.01.27; Published: 2020.02.10

Abstract

Magnetic fluid hyperthermia (MFH) treatment makes use of a suspension of superparamagnetic iron oxide nanoparticles, administered systemically or locally, in combination with an externally applied alternating magnetic field, to ablate target tissue by generating heat through a process called induction. The heat generated above the mammalian euthermic temperature of 37°C induces apoptotic cell death and/or enhances the susceptibility of the target tissue to other therapies such as radiation and chemotherapy. While most hyperthermia techniques currently in development are targeted towards cancer treatment, hyperthermia is also used to treat restenosis, to remove plaques, to ablate nerves and to alleviate pain by increasing regional blood flow. While RF hyperthermia can be directed invasively towards the site of treatment, non-invasive localization of heat through induction is challenging. In this review, we discuss recent progress in the field of RF magnetic fluid hyperthermia and introduce a new diagnostic imaging modality called magnetic particle imaging that allows for a focused theranostic approach encompassing treatment planning, treatment monitoring and spatially localized inductive heating.

Key words: Theranostics, RF hyperthermia, RF treatment planning, RF treatment monitoring, magnetic fluid hyperthermia, hyperthermia, Magnetic Particle Imaging, Magnetic Nanoparticles, Superparamagnetic Iron Oxide Nanoparticles, *in vivo* Tracking

Introduction

Thermal ablation is the process of increasing tissue temperature by applying heat (i.e., induced hyperthermia) to cause irreversible damage to a pathologic target. Thermal ablation is used routinely in medicine to treat heart arrhythmia, to cauterize the endometrial wall, to cauterize blood vessels, and to treat metastatic/recurrent tumors.

Numerous technologies have been developed to optimize the efficiency and localization of ablation inside the body, each with their strengths and weaknesses. One common technique, catheter-based radiofrequency (RF) ablation, utilizes an electrode mounted on a catheter to ablate nearby pathology. The catheter is placed near the pathology and utilizes RF currents in the range of 350–500 kHz to ablate local tissue. The energy is only deposited near the electrode and the size of the ablation zone is controlled by the quasistatic electromagnetic field patterns of the

electrodes, with some spatial variations due to the heterogeneity of tissue conductivity and permittivity. High intensity focused ultrasound (HIFU), another common technique, utilizes ultrasound energy applied via focused ultrasound transducers to cause an increase in temperature (sometimes with direct acoustic cavitation), eventually resulting in full tissue ablation. Here the size of the treatment zone (1–3 mm) depends on the frequency of the ultrasound beam (typically below 2 MHz) and the arrangement of the transducer arrays [3, 4]. Alternatively, the lesion can be cooled down to freezing or near–freezing temperature to bring about cell death as in cryotherapy.

Non–invasive imaging-guided treatment approaches are of benefit by not only localizing the tumor lesion, but also by facilitating for real–time treatment monitoring. Most common methods for imaging-guided treatments include, radiation delivery system using images from CT or PET-CT [5, 6], cryotherapy under real–time ultrasound and MRI guidance [7, 8], and HIFU under MRI guidance [9, 10].

Magnetic fluid hyperthermia (MFH), which is the use of an externally applied field to heat suspensions of iron oxide nanoparticles within the body, is a technique that has no fundamental depth limitation and has minimal heating of background tissues, owing to specific localization of the hysteretic heat to the iron nanoparticles. One of the first reported uses of MFH in medicine was for heating sentinel lymph nodes to treat metastatic tumors. Iron oxide nanoparticles were injected, such that they concentrated in the metastasized sentinel lymph nodes. Heating the nanoparticles by applying 100–300 kHz magnetic induction fields was thought to preferentially ablate metastatic tumors [11, 12]. The longer wavelength of the RF fields used in MFH makes it difficult to localize the energy towards a confined location in the human body.

Iron oxide nanoparticles (SPIO) with core sizes of 4–28 nm, show superparamagnetic behavior, with magnetic saturation comparable to that of a ferromagnet but with zero coercivity and zero remanence. These nanoparticles are used clinically for iron supplement therapy in anemic patients and as a magnetic resonance imaging (MRI) contrast agent. SPIOs for MRI are used as a negative contrast imaging agent especially targeting the reticuloendothelial system [13, 14], and more recently iron oxide nanoparticles developed to treat anemia are being evaluated for off-label use as positive MR contrast agent for angiography [15, 16]. MRI permits direct iron quantitation using relaxometry and susceptibility mapping approaches, however this is challenging due to the effects from magnetic field inhomogeneities, phase effect from the tissue composition and the overall ppm level sensitivity limit of the modality [17, 18].

Recently, these SPIOs have also found use in a new imaging modality, called magnetic particle imaging (MPI). Introduced by Gleich & Weizenecker in 2005 [19], MPI forms images by exploiting the intrinsic saturation property of SPIOs. MPI has numerous advantages for diagnosis and therapy. MPI only sees the magnetic tracers without obscuring signal from background tissues. Also, MPI has superb sensitivity of better than 1 micromolar iron [20-23]. MPI is reported to have the highest therapeutic cell tracking sensitivity of all positive-contrast imaging techniques, with a detection limit of 200 labeled cells [22]. More recently, it was shown that a high sensitivity of ~ 100 picogram per 1 mm^3 voxel sensitivity [24] could be achieved in combination with a high temporal resolution of 46 frames-per-second, for real-time perfusion imaging of stroke lesion [25] and to evaluate blood vessel response of tumors to treatment [26]. In addition to its high sensitivity and ideal contrast, MPI also has an excellent safety profile. Both the SPIO tracers and MPI scanners have no ionizing radiation, and many tracers have already been approved by the FDA or EU for safe human use [13, 27-29]. The SPIO remain superparamagnetic until hydrolyzed or enzymatically degraded, as demonstrated by months-long longitudinal in *vivo* MPI cell tracking studies [30, 31]. The SPIOs typically are cleared through the hepatobiliary system [14]. Lastly, MPI is fully quantitative with zero depth attenuation [32, 33] and allows for the quantification without view limitations. MPI is being developed in many academic labs including from Germany [19, 34, 35], Turkey [36], Japan [37], China [38], Canada [39, 40] and the USA [31, 41-45].

MPI complements imaging techniques of nuclear medicine. MPI tracers can be stored and used without prior preparation and lacks any complex radiochemistry. As just two examples, SPIOs targeted with macroaggregated albumin (MAA) could be injected directly from the refrigerator, with the first MPI scan in just a few minutes [46]. This would be much faster than traditional Tc99m-MAA studies with Scintigraphy or SPECT, which typically require 3 hours. Similar acceleration could also be obtained using MPI for diagnosing GI bleeds [47]. Several MPI applications [48, 49] have already been tested in rodent models including (see Figure 1): real-time MPI image-guidance of catheters [50, 51], stroke diagnosis [25], angiography [52], lung perfusion [46], lung ventilation [53-56], cancer imaging [2], cancer theranostics [55, 57], stem cell tracking [22,

30, 31, 44, 58], brain perfusion imaging [42, 59], magnetic hyperthermia [1, 60-62] and gut bleed detection [47].

In Magnetic Particle Imaging (MPI), an image is created by exciting the SPIOs located only at the field-free region (FFR) [63, 64]. An FFR is created using strong magnetic field gradients in the order of 7Tm−1 in current preclinical scanners [2, 47]. By rastering the FFR in space, SPIO distribution can be localized by the instantaneous knowledge of the FFR and the signal obtained. In a similar manner, we have recently developed a localized MFH approach, where using gradient magnetic field, heating of SPIO particles can be achieved only at the location of the FFR [1, 65, 66]. The linear quantitative nature of MPI in combination with the localizing MFH treatment has great potential towards precision theranostics. In this review, we detail recent progress in RF based magnetic fluid hyperthermia (MFH) and its applications in ablation and controlled drug delivery. We will compare recent trends in image guided, *localized* MFH with MPI. Finally, we will also discuss techniques for thermometry and dosimetry for MFH.

Introduction to MFH, SAR and PNS limits

MFH uses VLF (very low frequency) or RF (radiofrequency) magnetic fields, which induce electric fields and ionic currents within the body. Because these fields can heat or stimulate nerves in the human body, there are safe operating rules prescribed by both the EU and FDA [67, 68]. In particular, there are limits to the E-field, to prevent peripheral nerve stimulation (PNS) and to Specific Absorption Rate (heating), measured in Watts per kg (W/kg).

The specific absorption rate (SAR) is a measure of the power dissipated in a biological sample, and is limited by the United States Food and Drug Administration (FDA) as described in Table 1. [69] It is defined as:

$$\mathrm{SAR} = \frac{\text{Total RF energy dissipated in sample (J)}}{\text{Exposure time (s)} \cdot \text{Sample weight (kg)}} \ (\mathrm{W/kg})$$

Table 1. FDA SAR limits for each organ. [69]

Tissue	FDA SAR Limit
whole body	0.4 W/kg
head	3.2 W/kg
any 1 g of tissue	8.0 W/kg

SAR is defined as the amount of energy deposited per unit mass of the tissue [70]. SAR can be simplified and measured as a change in temperature (T) over a short period of RF exposure (t) ($\Delta T/\Delta t$). Restricting SAR is essential to prevent a rise in the whole-body temperature. SAR can be computed using straight-forward quasi-static electric field simulators (accurate below 128 MHz) or it can be measured through calorimetric methods. SAR is often estimated *in vitro* using conductive tissue phantoms replicating the geometry of the human body. Because the specific heat of tissue is 4.2 J/(g°C), the maximum SAR limit of 4 W/kg is designed to ensure that rate of temperature rise rate remains safe.

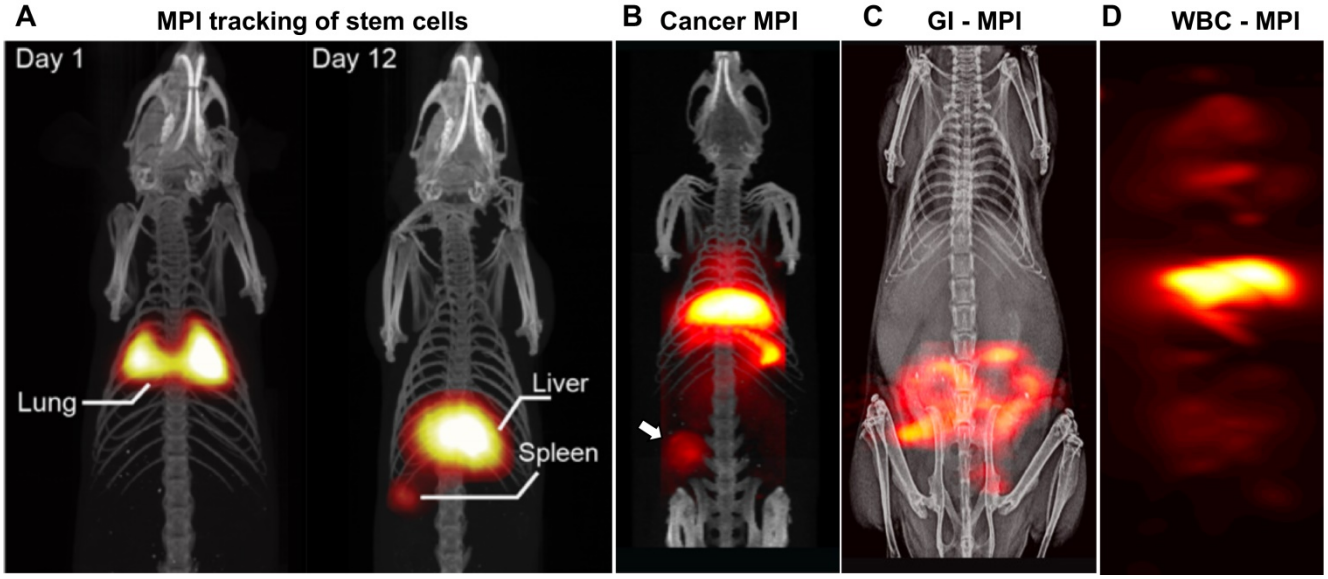

Figure 1: UC Berkeley MPI Data. (A) First in vivo tracking of stem cells using MPI, which has zero signal attenuation with depth and zero background signal (reproduced from [22] under creative common license). (B) First in vivo MPI images of triple negative breast cancer (Reproduced with permission from Yu E et al, [2] Copyright 2017 American Chemical Society) (C) First in vivo MPI study of gastrointestinal bleed assessment in a murine model, akin to Tc99m-RBC scans but without radiation (Adapted with permission from Yu E et al, [47] Copyright 2017 American Chemical Society) with 10-times greater sensitivity than RBC scintigraphy. (D) Monoclonal IgG-antibody functionalized SPIO MPI scan showing distribution of in situ labeled WBCs in the RES system of liver, spleen and marrow.

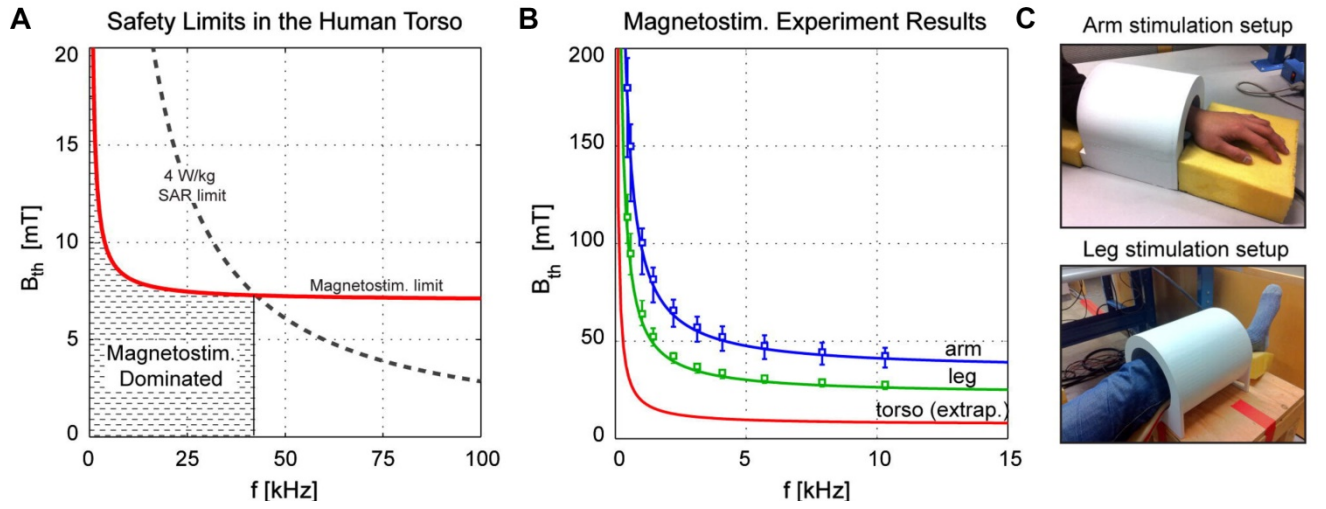

Figure 2: (A) SAR & PNS safety limit dependence on RF Frequency and amplitude as in a human torso, (B) magnetostimulation measurements in human arms and torsos [32]. PNS is the dominant safety concern for MPI at drive field frequency <42 kHz. (C) Measurement setup for assessing the stimulation limits as in (B). Reproduced with permission from Saritas et al., J Magn. Reson. (2013)[32] Copyright 2014 Elsevier.

PNS causes a sensory response in the muscle, described as a tingling, poking or twitching sensation. It is attributed to the electric field induced across neurons due to an applied oscillating magnetic field (magnetostimulation). Saritas et. al [32, 71] estimated the field amplitude and frequency dependence of the magnetostimulation effect in human arm and leg. Figure 2 explains the SAR and PNS threshold in humans. Based on the fundamental law of magnetostimulation [72], Saritas estimated that at lower frequencies of RF, the predominant safety issue in MPI is magnetostimulation. It is critical to understand the SAR and PNS limits in the design and implementation of RF hyperthermia. The readers are also referred to a comprehensive text book on RF interaction with biological material for more details [73].

Iron Oxide Nanoparticles for Magnetic Fluid Hyperthermia

Superparamagnetic iron oxide (SPIO) nanoparticles used as tracers for MPI can also be used for MFH. The heat generated by SPIOs in response to an oscillating RF field is due to Brownian rotational or hysteretic loss of the nanoparticles and is dependent on the frequency of the oscillating magnetic field. The heating characteristics of the nanoparticles are also measured in the units of specific-absorption rate (SAR) similar to that of biological tissue heating. Intrinsic loss parameter (ILP), a property of the iron oxide nanoparticle, was pro- posed as a method to normalize SAR values measured at different magnetic field amplitudes and frequencies. The ILP is defined as the power loss dependence on the frequency and amplitude of the applied field and is defined in units of nH m^2 kg^{-1}. SAR and ILP are often interchangeably used as a measure of power deposition [74].

Rosensweig [75] provided an analytical basis for magnetic nanoparticles heating in an oscillating field. SPIO exhibit a uniaxial anisotropy, and an energy barrier exists along this axis. Magnetization of SPIO changes with the applied field with the relaxation time constant, $\tau^{-1} = \tau_{\text{Brownian}}^{-1} + \tau_{\text{Néelian}}^{-1}$. The Néel time ($\tau_{\text{Néelian}}$) constant refers to the time for the internal magnetic moment to align with the external magnetic field which is affected by the interdomain interaction within the particles, whereas the Brownian time (τ_{Brownian}) constant defines the rotational time that the entire particle goes through with respect to the external magnetic field and is affected by the local micro environment. Though the Néel and Brownian relaxation coexist, in general, small core size SPIO particles can be considered as Néel relaxation dominant and large core size SPIO particles as Brownian relaxation dominant [75].

According to Rosensweig equation, the power dissipation, P, can be defined as: $P = \pi\mu_0\chi_0 H^2 f \frac{2\pi f\tau}{(1+2\pi f\tau)^2}$. Where, P is dependent on the relaxation time constant τ, applied frequency f, the square of the applied field amplitude H and χ_0, the actual chord susceptibility which in this equation corresponds to the Langevin equation. From the equation it can be observed that the heating gains can be high if the frequency is greater for τ.

At higher frequencies of applied external fields, the SPIO particles show hysteresis. The frequency below which a particle behaves superparamagnetic is referred to as the blocking frequency [76, 77]. Above the blocking frequency, heating due to hysteresis loss is observed, as shown in Figure 3. The blocking frequency and heating characteristics are influenced

by the particle size, shape, particle dispersity and the viscosity of the surrounding media.

Tay et al. used 13-nm core iron oxide nanoparticles coated with poly-ethylene glycol and reported no rise in temperature of the solution containing particles subjected to a 20 mT, 20 kHz alternating magnetic field (a frequency typically used for imaging in MPI). The same particles demonstrated a SAR of 120 W/kg of tissue at a 354 kHz and 13 mT field amplitude [1].

Shape anisotropy in nanoparticles can improve their heating properties [78, 79]. Khurshid et al. reported a 1.4-fold improvement in the particle SAR for cubic iron oxide nanoparticles compared to spherical particles [80]. The cubic particles had a 1.5-fold increase in effective anisotropy field compared to spherical particles. SAR improvement of nanoparticles can also be achieved by controlling their size. Sheng Tong et al. demonstrated the hysteresis loss of nanoparticles increases with particle size from 11–33 nm and saturates at sizes > 33 nm [81]. Aggregation of nanoparticles can also result in better heating performance due to increased anisotropy resulting from dipole interaction from between the neighboring particles under the influence of the applied field [82-86]. Doping ferrite with anisotropic material such as cobalt, zinc, nickel or manganese can also improve the heating property of the materials by increasing the overall anisotropy [87-89].

Rosensweig [75] further discussed the effect of viscosity and particle dispersity on the heating characteristics of SPIO. The Brownian relaxation constant (in the case of large size particle) especially seems to be strongly dependent on the viscosity of the matrix fluid, with better heating characteristics with increasing excitation field frequency at a given viscosity. Whereas, polydispersity can degrade heat production of the nanoparticle. Dennis CL & Ivkov R, in their work [90] derive the effect of polydispersity from the Chantrell equation [91], where by accounting for polydispersity in the lognormal distribution of particles, the heat generated can be assumed to be distributed broadly over the size distribution of the particles. There appears to be a scarcity on experimental work reporting the influence of viscosity and polydispersity of SPIO for MFH [90, 92]. This can be attributed to the complex interplay of various nanoparticle parameters such as zeta potential, surface coating, solvation chemistry, configuration of the particle coating and particle-protein interaction; all of which can have a profound effect on the colloidal stability of the particle system.

Coating material apart from imparting biocompatibility on SPIO can also affect the heating performance. To a first degree Jordan A et al., [93] noticed a difference in SAR between dextran coated and aminosilan coated iron oxide nanoparticles, with aminosilan particles having 1.2 fold better SAR than dextran coated particles, with silane coated showing better malignant tumor cell labeling. Liu XL et al., in their work [94], performed a systemic analysis of SAR using SPIO coated with different molecular weight PEG, and observed an increase in SAR with decrease in the thickness of the surface coating, attributing to the dominance of Brownian relaxation based heat losses. However, the reduced thickness can also affect the colloidal stability of the particles that is also affecting the SAR measurement. Further, the heating performance was also noticed to depend on the thermal conductivity of the coating [85, 94]. The effect of coating material and SAR was also observed to have intrinsic dependence in the solvent in which the particles were suspended, the zeta potential defining the colloidal stability, and the amount of the coating material around the nanoparticles.

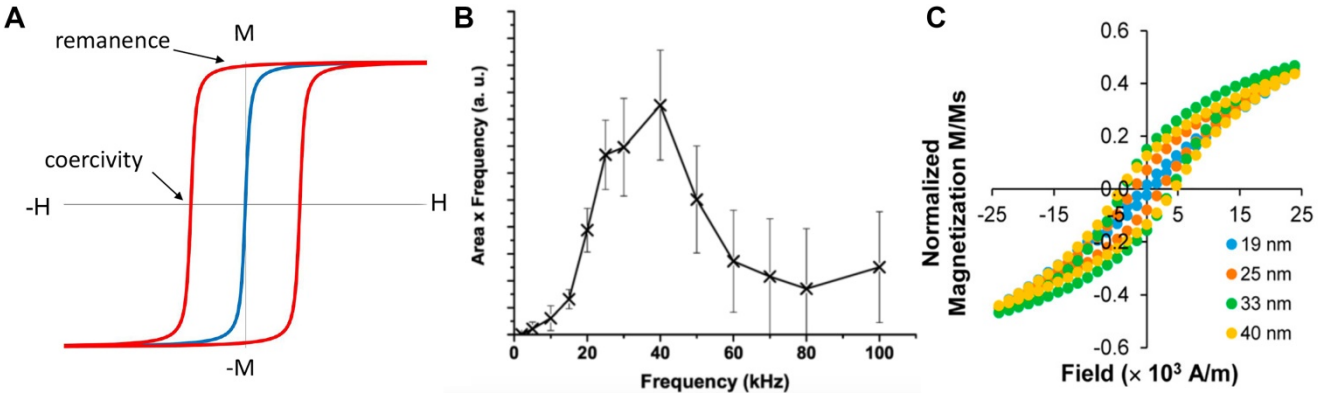

Figure 3: SPIOs obey Langevin physics. (A) Within an applied field (positive or negative) the particles align in the direction of the field. Once the field is removed the net magnetization becomes zero (blue). However, relaxation delays (similar to hysteresis) are observed when the applied field is oscillated at higher frequencies (red). Heat is generated as a result of hysteresis loss and is proportional to the area within the hysteresis loop. The heat generated in SPIO is a function of frequency and applied field. Figure (B) shows the hysteresis response of clustered Chemicell FluidmagD particles at different oscillating field frequencies. Note that the hysteric loop opens at 2 kHz. Reproduced with permission from [77] Copyright 2007 IEEE. (C) Hysteresis is dependent on the size of the SPIO particles and greater heating can be achieved with larger particles. Adapted with permission from Tong S et al., ACS Nano. [81]. Copyright 2017 American Chemical Society.

MPI resolution and sensitivity is also dependent on the SPIO characteristics, with 24-28 nm core size SPIO particle providing the optimal resolution and sensitivity for MPI, any further increase in size caused blurring of images in MPI [95]. Currently, the LodeSpin particles provide the best resolution in the order of 0.8 mm and detection sensitivity of about 3 ng of Fe [48]. The effect of MPI drive field amplitude and frequency on the particle size ranging from 18-32 nm was investigated by Tay ZW et al [96]. In this work, a systematic optimization effort was carried out to identify ideal operational conditions for MPI resolution and sensitivity characteristics over a range of nanoparticle sizes. A striking difference was observed between two groups of particle (a) small core size particles (18-24 nm) and (b) large core size particles (27 & 32 nm) with two optimal operation conditions, 70 kHz and 5 mT (for smaller core particles) and 1 kHz and 14 mT (for large core particles).

MPI images are acquired in partial field-of-view segments [33, 71, 97], as a result of which the particles do not heat up, unlike continuous excitation in MFH. Also, new pulsed MPI approaches can mitigate hysteresis loss from SPIO particles [98]. We propose a size range of 24-28 nm would be optimal for both MPI and MFH. Further SPIO configuration such as chaining and aggregation that increases the anisotropy would be interesting to evaluate for combined MPI and MFH. On the other hand, smaller size particle might provide poorer resolution and sensitivity in MPI and weaker hysteresis loss for MFH [99].

Delivering adequate dosage of nanoparticles to tumors for MFH is still particularly challenging, with almost all i.v. administered nanoparticle system relying on the enhanced permeation and retention phenomenon (EPR) of the tumor for targeting, of which only 0.7% median dose of nanoparticles makes its way into the tumor vicinity [100]. Since SAR is a function of the concentration of SPIO particles in MFH, large quantities of SPIO must be present in the vicinity of the tumor. This is achieved by an intra-tumoral administration of the prepared nanoparticles. Currently, NanoTherm® iron oxide nanoparticles produced by MagForce Nanotechnologies GmBH are available for clinical use in the European Union. NanoTherm® is composed of 12 nm core size nanoparticles with a bio-compatible aminosilane coating. The solution is available at a very high concentration of 112 mg/mL of iron [101] relative to Feridex *i.v.* solution's concentration of 11.2 mg Fe/mL [102]. The difference in concentrations of the parenteral preparation for the therapeutic versus diagnostic purposes is because a large localized concentration of iron oxide is required to achieve reasonable heating to ablate tissues. For MFH, the particles are administered locally by a stereotaxic procedure and the aminosilane coating ensures strong interaction between the target tissue and particles, Figure 4C.

MFH treatment

Given the safety limits of RF fields imposed by human SAR and PNS, it is common for MFH researchers to employ relatively high concentrations of nanoparticles to allow for heating of the target tissue. To achieve a therapeutic response in tissues using hyperthermia, two treatment approaches are used. In the first approach the temperature of the target tissue is raised to 40–45°C and held for a defined amount of time causing changes and cellular death, and in the second approach the tissue is completely ablated at a higher temperature of 75–90°C.

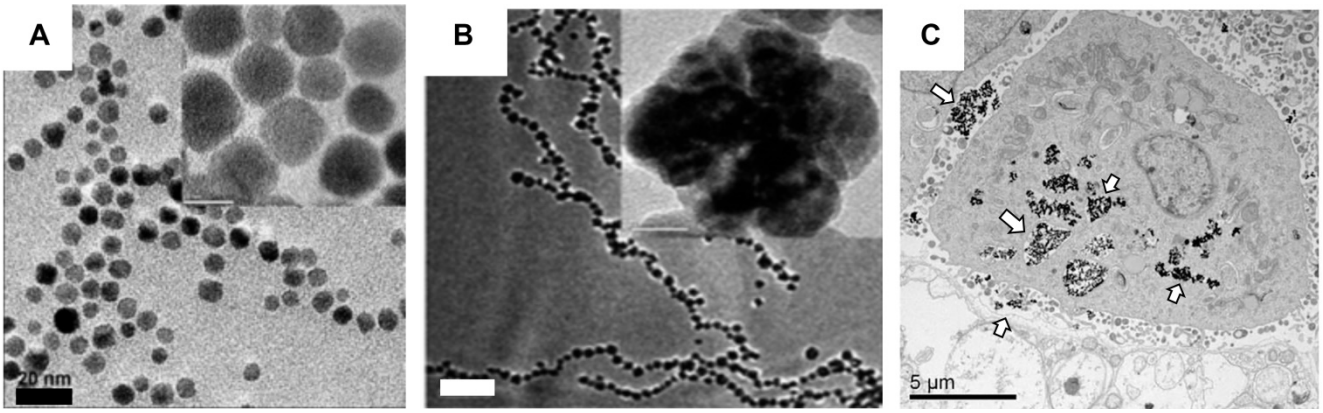

Figure 4: Clinically used SPIO for MFH consist of aminosilane surface modified 10 nm iron oxide nanoparticles. (A) TEM images of 3–aminopropyltriethoxysilane coated iron oxide particles that are highly mono-disperse (scale bar = 20 nm)(Reproduced with permission from [101] Copyright 2010 IEEE) (B) Aggregated and chained nanoparticle configurations can improve the effective SAR value (500 W g^{-1} at 89 kA m^{-1} AC magnetic field and 240 kHz frequency)) (scale bar = 200 nm). Reproduced with permission from [102] Copyright 2011 The Royal Society of Chemistry. (C) TEM images reveal the aminosilane coated nanoparticles are endocytosed and adhere strongly on the surface of the cancerous cells (arrows), greatly increasing the chances of localizing the heat (scale bar = 5 µm) [103, 104] (Reproduced with permission from [106] Copyright 2019 Elsevier).

Ablation techniques are used in the clinics and mostly applied locally using a catheter-based approach. Ablation technique requires short tissue exposure time to high temperatures and can lead to what is referred to as coagulative necrosis. Apart from RF based ablation approach, focused ultrasound achieves localized temperature of ablation. A whole-body exposure to temperatures of ablation will not be tolerable by humans.

A biological material can be considered as a dielectric media comprising of large amount of water, ions (sodium, potassium and calcium) and macromolecules (proteins, fat and com- plex sugar). Heat from hyperthermia can cause molecular and physiological change in the tissue. At the molecular level, heating causes conformational changes in macromolecular proteins and DNA resulting in impaired cellular function, causing senescence, apoptosis and necrosis [105, 106]. Heat shock proteins, that are over expressed in cells during physical stress and injury, including exposure to hyperthermia, elicit anti-tumor activity [107]. There is evidence that an increase in infiltration of antigen presenting cells occurs during hyperthermia, causing cytotoxic immune responses in the tumor [108]. Moreover, other physiological changes in tumor such as an increase in blood perfusion and altered metabolism, as a result of hyperthermia can sensitize tumor for combinatorial therapy such as chemotherapy and radiation therapy [109]. Newer research suggest that the therapeutic response due to RF field may be brought about by mechanically actuated deformation and shredding of SPIO bound proteins in the intra-cellular milieu of cancer cells [110, 111]. This would require a sub-optimal rise in temperature and greatly reduce the exposure of patient to RF excitation. The underlying mechanism of biological cell death as a result of shredding requires further investigation.

To measure the effective thermal dose delivered via hyperthermia, the cumulative equivalent minutes at 43°C (CEM43°C) was proposed in 1984 by Sapareto and Dewey [112, 113]. The CEM43°C allowed for the standardization of thermal dose across publications to a common unit by converting any time-temperature history into equivalent number of minutes of heating at 43°C and is defined as, $\mathrm{CEM43^{o}C} = \sum_{i=1}^{n} t_i R^{(43-T_i)}$, where t_i is the i-th time interval, T is the average temperature during time interval ti and R is related to the temperature dependence of the rate of cell death (R(T < 43°C)=1/4, R(T> 43°C)=1/2). R is a measure of several factors associated with cell death and is influenced by the parameters discussed above.

The effect of heat in biological tissue is comparable to that of radiation exposure [114]. The surrounding pH of the target tissue, the metabolic state and blood flow (hypoxic versus normoxic) conditions all affect the response of the tissue to heat. In certain circumstances, the tissue can generate a thermotolerance: a state where the cells become resistant to heat. Heat shock protein provides protection to the cells and tissue during physical stress. Repeated exposure to physical stress will allow for tolerance development. The heat shock proteins act specifically by managing protein synthesis, allowing for permeability changes to resist heat exposure, and reduce cytokine related stress mediated inflammation [115-117]. Mechanistically the thermotolerance was related to the expression, accumulation and relative half-lives of the heat shock proteins. The tissue of interest must lose the tolerance before it can be treated.

Thermotolerance is a key issue during MFH, which reduces effective killing by 4-10 folds. Cells take up to 100 hours to lose their sensitivity to thermotolerance [112-114]. It is estimated that to effectively treat a tumor, at least 90% of the tumor should receive a CEM43 of 25 [118]. Thus, a long duration of hyperthermia is needed in order to achieve effective treatment. To reduce the duration of treatment, MFH is administered in combination with radiation therapy. Heating improves the sensitivity of the cancer cells to radiation and reduces the treatment time needed [119].

Clinical Systems for MFH

Clinical MFH based pilot studies have been carried out in treating prostate and recurrent brain tumors in humans. The first reported use of MFH, was in a patient unresponsive to high dose brachytherapy for a T3 prostate carcinoma [120]. The overall treatment procedure was divided into three parts. The treatment of solid prostate tumor was first evaluated using non-invasive CT imaging. Treatment planning was then carried out based on the CT images. Parameters such as the particle dose needed, the site of particle placement, and the corresponding SAR with the applied field were estimated using simple numerical methods, that accounted for tumor margins, environment surrounding the tumor and blood supply to the tumor (that can act as a heat sink). Finally, a dose of 12.5 mL of iron oxide fluid was injected into 35 mL prostate organ using a trans-urethral catheter under ultrasound guidance. Hyperthermia was applied using an RF applicator. The authors of this clinical study noticed patient discomfort and pain during RF application and had to temporarily reduce the applied field.

In another clinical evaluation, MFH was carried out in combination with radiation therapy in treating an aggressive recurrent brain tumor (glioblastoma) [119], once again divided into three parts. In the first part, the patients underwent surgery to remove tumors and had SPIO particles administered stereotactically. Secondly, MRI and CT images were acquired to image the particle distribution and a forward model was applied to estimate the heating boundaries. Finally, combined MFH and radiation therapy was used for treatment.

In both clinical studies, hyperthermia treatment was carried out with an implanted thermometric probe to measure the heat generated [121]. The latter clinical trial reported no side effects and in combination with radiation improved the overall survival of patients with first recurrence of the brain tumors.

The clinical magnetic hyperthermia system used in the glioblastoma clinical study was built at MFH Hyperthermiesysteme GmbH. While technical information about the clinical hyperthermia systems used is limited, there are several papers describing how the clinical systems were developed [122, 123]. The largest difference between a small animal system and clinical system is the coils to generate the alternating magnetic fields required for MFH. In a small animal system, both air-core and ferromagnetic-core coils can be used to generate alternating magnetic fields [123]. However, air-core coils cannot be used in clinical scanners due to the size of the operating area, as generating sufficient magnetic field strength over large areas using these cores requires excessive power.

The high current and voltage in air-core coils also introduce safety concerns [123]. Hence, in clinical systems ferromagnetic-core coils are used to minimize the power consumption and lower the power and voltage across the coils. The schematic of a clinical magnetic hyperthermia system is shown in Figure 5.

The magnetic field in the operation area is generated by two ferromagnetic-core coils (Figure 5 A-B). The field strength is adjustable from 0 to 15 kA/m corresponding to 0 to 20 mT [122]. Homogeneity of the magnetic field is essential for equal heating of the treatment area. The clinical systems can realize 90% transverse homogeneity within a 20 cm range as shown in Figure 5B [123].

As discussed previously, clinical studies have strongly relied on CT images and MRI for estimating the nanoparticle distribution and for treatment planning. These imaging modalities have difficulty in accurately estimating treatment SAR. The difficulty with using X-ray CT for visualizing iron oxide is that, a considerably high iron content will be needed for any discernible signal in CT, whereas higher iron oxide nanoparticles concentration in MRI cannot be accurately estimated [104, 120, 122].

Introduction to Magnetic Particle Imaging for localized MFH

MPI is a new and evolving tracer imaging modality with distinct imaging physics from all other imaging modalities—including MRI. MPI images the intense electronic magnetization of SPIOs (600 mT), which is 100-million-fold more intense than the nuclear paramagnetism of water at 1.5T, which has nuclear susceptibility 3.8 ppb [124]. Importantly, it is not possible to obtain an MPI scan within an MRI scanner. Instead, an MPI scanner uses a very strong gradient magnetic field (current preclinical scanners use up to 7 T/m) to generate a field-free region (FFR) as shown in Figure 6 that is rastered across in space to generate images of superparamagnetic iron oxide nanoparticle tracers. The FFR occurs at the center of two or more magnets designed to create a field gradient.

Within the FFR, SPIO particles experience minimal magnetic fields, and are free to rotate under the influence of a weaker 20–40 kHz excitation field. Outside of the FFR, particles are locked to the strong fields lines of the gradient and are hence unable to rotate. In combination with the FFR and the Langevin behavior of the SPIO, it is possible to create an image of the location of SPIO in space [2, 19, 32, 33, 47, 64, 125].

The homogeneity requirements of MPI are modest: about 1% in-homogeneity is well tolerated in the selection field gradient, which is several orders of magnitude less stringent than the 1 ppm homogeneity required for MRI. Indeed, this explains why MPI images of the lung are completely unaffected by the 10 ppm field variations due to air-tissue interfaces. Many MRI pulse sequences fail in the lung due to short T2* times.

A long-standing challenge in the MFH field is localizing the heating to a precise target deep within the body. This is important because the nonspecific uptake of SPIOs to the liver, kidney and spleen typically exceeds the specific uptake to the tumor. Unfortunately, it is not possible to focus 300 kHz magnetic fields to avoid heating the liver, because the wavelength of 300 kHz magnetic fields is longer than 100 meters in vivo. Hence, current techniques for MFH pose a risk of heating the liver when we wish to ablate only a tumor. To address this important technical challenge, we exploited the MPI gradient field to localize MFH heating [1, 60, 65, 66]. Here, despite using a 300 kHz magnetic field, we were able to localize heating to a small region of space, roughly

the size of a grain of rice or just a few millimeters in size. Akin to MPI, we used a gradient magnetic field to prevent heating of SPIOs outside the FFR region. Only the SPIOs inside the FFR can rotate and thereby undergo induction heating, as shown in Figure 6.

Recent Innovations using combined MPI-MFH

Magnetic particle imaging has opened a new venue for localized MFH treatment. The field-free region (FFR) used to generate images in MPI can also be used to spatially localize heat only at the point of FFR with minimal heating elsewhere. Dhavalikar et al. discussed the theoretical basis of localized MFH using FFR [66]. Bauer et al., first demonstrated localized heating of nanoparticles in 1D using a gradient field generated with a permanent magnet [41]. While, Hensley & Tay et al. [1, 60, 65] developed the first 2.3 T/m magnetic gradient localized MFH system, capable of selectively heating SPIO particles separated by a distance of 7 mm (Figure 6E & F). The localized MFH system consists of two permanent magnets with poles facing each other resulting in a field free region (Figure 5C). The field free region can

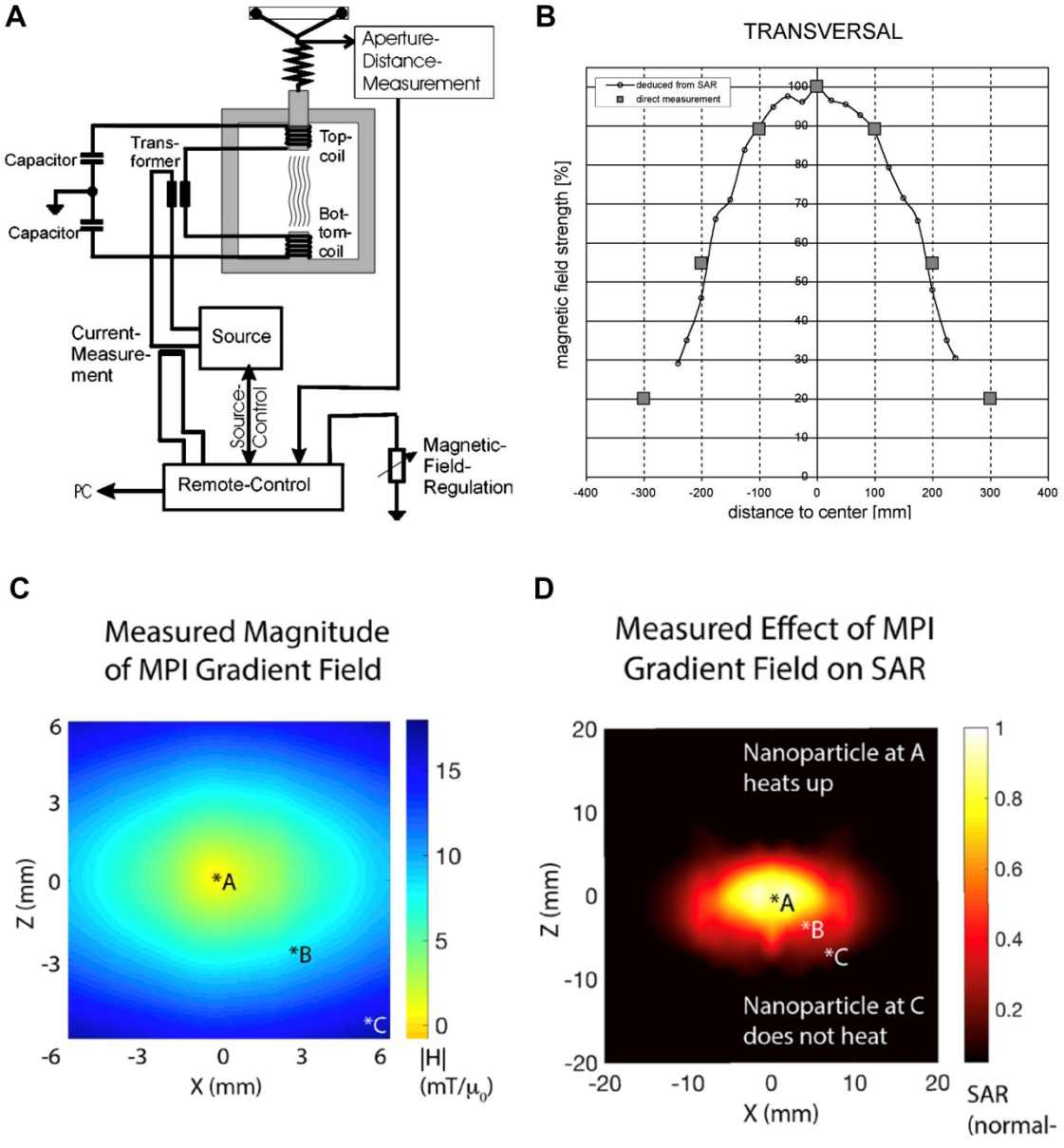

Figure 5: Commercial hyperthermia systems: (A) A clinical MFH 300F hyperthermia system [122] consists of a resonating circuit at a ferrite yoke that generate an oscillating field of 100 kHz between the pole shoes above and beneath the treatment aperture. The setup can be adjusted to limit the exposure of oscillating magnetic field exposure on the patient and (B) its corresponding field homogeneity in the transverse direction [122]. The patient is slid through the aperture and the aperture distance controls the effective area of exposure and the field can be adjusted by adjusting the current to the coils. (Reproduced with Permission from [122], Copyright 2004 Wiley & sons) (C) Localized hyperthermia system with 2.3T/m field-free line gradient developed using permanent magnets at UC Berkeley [1, 60], and (D) its measured heating area of 7 mm diameter. The particles in zone *A heat up the most, with steep fall off at zones *B and *C. (Reproduced with permission from [1], Copyright 2018 American Chemical Society).

be moved anywhere within the patient and selective heating can be achieved. The size of the FFR can be varied by varying the strength of the magnetic field gradient. Thereby catering to the size of the lesion to be treated. A water-cooled copper solenoid coil was used to excite the nanoparticle at frequencies of 300kHz to generate heat. The measured SAR in the field gradient for a 11 nm SPIO particles coated with polyethylene glycol is shown in Figure 5D. From Figure 5D it can be observed that the heat from the particle is confined to a zone of 7 mm in diameter.

MFH requires robust treatment planning and it is essential to quantify the particle deposits at the site of the tumor for accurate SAR prediction and for subsequent treatment [123]. MPI has a broad dynamic range and is able to detect and quantify SPIO particles from few nanograms to several milligrams [30, 97].

In our recent work, MFH guided through MPI was studied *in vivo* [1]. MPI can accurately quantify the amount of iron oxide administered and predict the amount of thermal dose that can be deposited in the target tissue using a forward model workflow (Figure 7) [1]. The SAR estimate was linear with the mass of the iron oxide nanoparticles, Figure 8A. Once the particle distribution and SAR are predicted, a spatial filter can then be applied, by moving the FFR in space to the appropriate location, at which hyperthermia is to be applied. Finally, the RF excitation can be tuned and controlled based on the temperature change required and maintained for adequate heating.

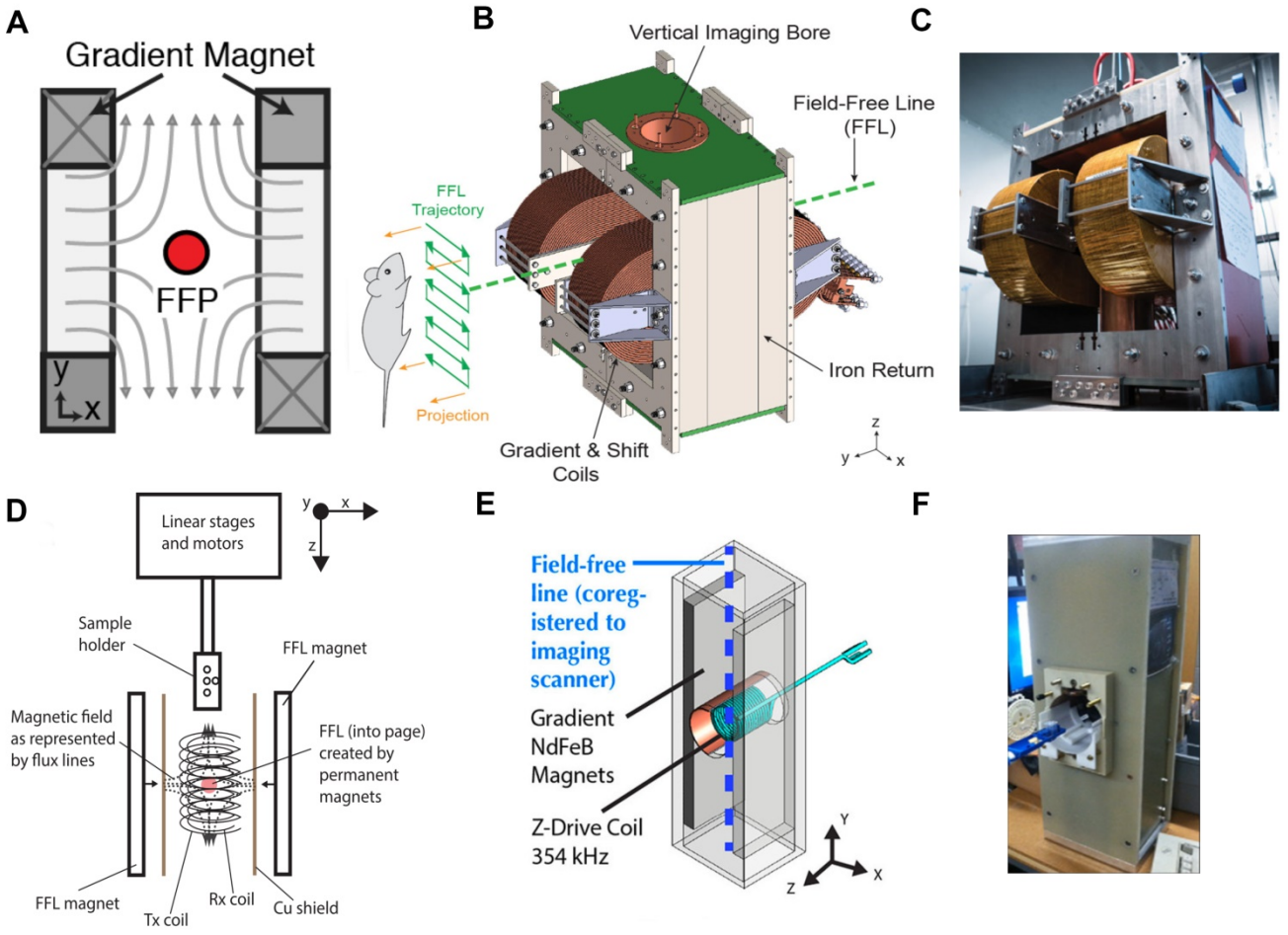

Figure 6: Magnetic Particle Imaging (MPI) uses a (A) gradient magnet to create a field-free-region (FFR). The FFR can be a point (field-free point or FFP) or a line (field-free line or FFL) in space. Magnetic nanoparticles at the FFR are free to rotate and oscillate in response to low (20-40 kHz, very low frequency range) excitation fields, while particles away from the FFR are locked due to the magnetic field. The induced magnetization from the particles in the FFR can be picked up by sensitive coils using Faraday's principle of induction. By rastering the FFR across the entire field-of-view, an image indicating the quantity and spatial location of the nanoparticle tracer can be produced. (B) An engineering design diagram of an FFL MPI scanner and an MPI scanner at UC Berkeley [47] (Reproduced with permission from Yu E et al, Copyright 2017 American Chemical Society)(C) the UC Berkeley FFL scanner has two electromagnets, and the FFL trajectory can be rastered in space by controlling the current through the electromagnets. 3D images can be obtained using tomographic reconstruction algorithms. (Reproduced with permission from Yu E et al, Copyright 2017 American Chemical Society) (D) The same principle of MPI can be applied to localize particle heating (spatially controlled Magnetic Fluid Hyperthermia) only at the FFR. Using a gradient magnet and RF coil operating at higher excitation frequency (354 kHz), spatial control of particle excitation can be achieved (Reproduced with permission from [60], IOP Publishing. Copyright Institute of Physics and Engineering in Medicine. All rights reserved) (E) & (F) engineering design diagram and an image of a field-free-line Magnetic Hyperthermia setup at UC Berkeley. (Reproduced with permission from [1], Copyright 2018 American Chemical Society).

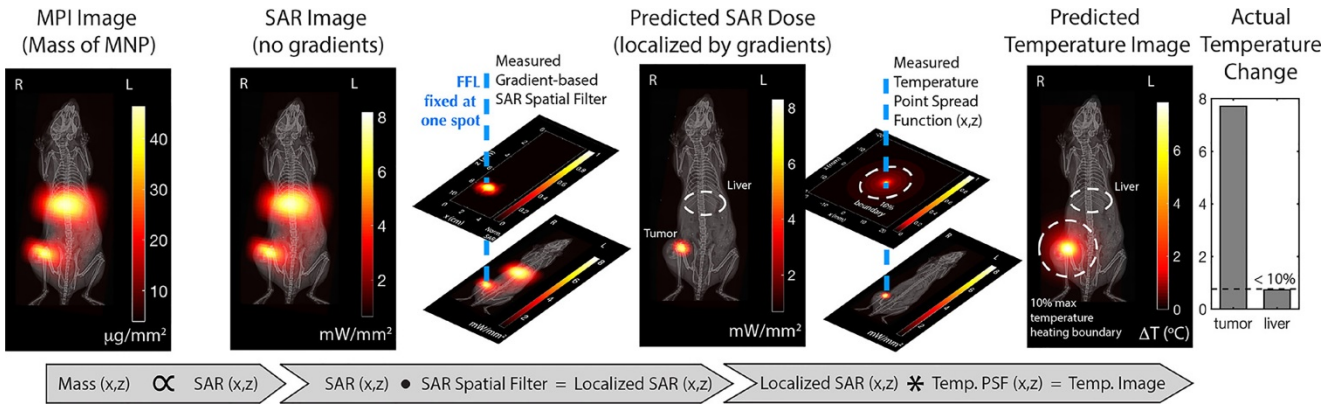

Figure 7: MPI image guided MFH Treatment design planning proposed by Tay et al. [1] MPI enables precise spatial quantification of the amount of SPIO particles administered and the gradient system enables control of the spatial zone to which RF is applied. Based on a prior knowledge of the particle response to the field, a temperature map can be generated. (Reproduced with permission from [1], Copyright 2018 American Chemical Society).

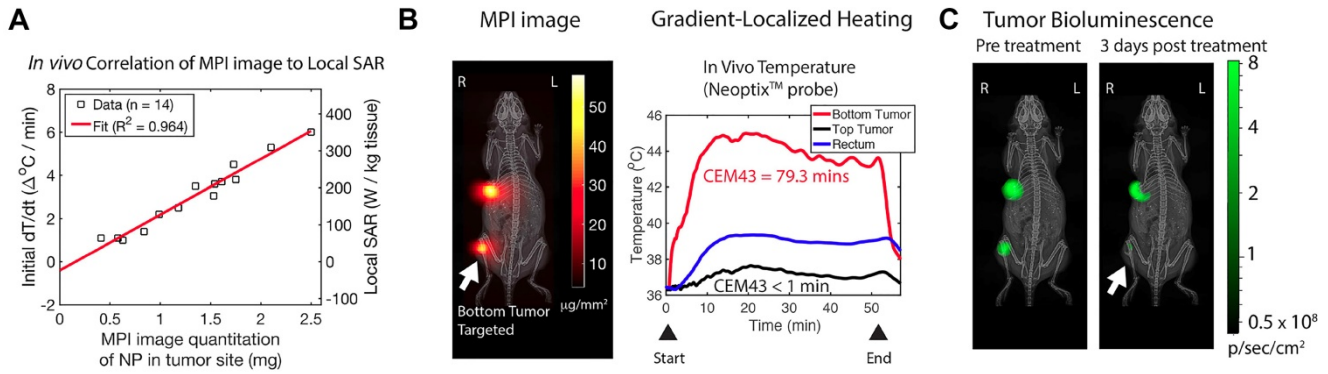

Figure 8: In *vivo* localized MPI guided MFH experiment. (A) MPI images provided quantitative information of SAR estimate at the tumor site Tay ZW et al. [1] (B) Using a 2.3 T/m magnetic field gradients, the FFR was localized towards the bottom tumor of a dual tumor xenograft mouse model and (C) a thermal probe was used to estimate CEM43 of 80 minutes that was achieved using RF excitation of the nanoparticles. (D) The bio-luminescence activity after treatment confirmed selective growth inhibition of the treated bottom tumor compared to untreated top tumor. (Reproduced with permission from [1], Copyright 2018 American Chemical Society).

The workflow described above was evaluated in a murine model with dual tumor xenograft of human origin. Figure 8B shows the in vivo distribution of iron oxide nanoparticles that were intratumorally injected and imaged using MPI. The FFR was positioned on one of the tumors (bottom) and was heated to a CEM43 of 79.3 minutes (measured using an optical fiber thermal probe) while the particles in the other tumor (top) did not respond to RF excitation. The overall body temperature of the mouse was not affected (based on rectal temperature measurement). The treatment was confirmed by a reduced bio-luminescent activity indicative of tissue death, Figure 8C. This demonstrated the localized treatment of tumors, while sparing other tissues like the liver, which typically shows high non-specific SPIO uptake [1, 60]. Though, it is unclear at this stage if the RF interaction with biological tissue outside the FFR can cause burns, this first study did not report any side effects nor any non-specific rise in temperature in the murine model as a result of applied RF fields.

Recently, newer designs for the FFR are being investigated [126] that can be tuned to cater the shape of the tumor to be treated. MPI guided MFH was reported in another study by Du et al. The authors achieved tumor targeting and particle retention by targeting the fibrin-fibronectin complexes, that are over expressed in tumor interstitium, using SPIO with surface functionalized small molecule peptide, CREKA [38]. They also reported a quantitative comparison between MRI and MPI. MRI was found to have much more difficulty in quantifying iron oxide tracers than MPI, as iron oxide tracers generated negative contrast in MRI versus positive signal in MPI. Finally, the authors were able to ablate the tumor using RF excitation.

Treatment dose in MFH is monitored as a function of rise in temperature. Current techniques involve the use of optical-fiber probes or infra-red cameras to measure the temperature changes. The latter is used when positioning the optical fiber probe is precluded by difficulty and invasiveness. Non-invasive imaging tools are being evaluated for treatment monitoring during hyperthermia. A rich area of innovation is measuring the temperature change during hyperthermia treatment, as it is of utmost importance for safe and effective treatment.

MRI can measure temperature changes based on a subtle shift in proton resonance frequency (10 ppb/degree C) [127-129]. MRI thermometry has been combined with HIFU for cancer theranostics and for pain management [128, 130]. With high-resolution spatio-temporal information from MRI and the ability for real time monitoring, MRI can help to precisely determine HIFU treatment and monitor its course.

It is possible to extend MPI technique towards real-time temperature monitoring. SPIOs used in MPI and MFH, respond to an RF excitation through a relaxation process dependent on the dominant behavior of the particles, i.e., Brownian and N´eel relaxation. Brownian relaxation can be considered as the time for the entire particle to rotate or flip in response to the excitation field and is influenced by the immediate surrounding or the micro-environment of the particles, while N´eel relaxation can be considered as a time constant for the internal flip in magnetization of the particles under the influence of the excitation field without any physical rotation [131-133]. The relaxation times of SPIOs may provide information about the temperature or viscosity of the surrounding fluid in the vicinity of the SPIO [36, 51, 134, 135]. Recently Weaver et al. proposed a method to measure the local micro-environment temperature of the administered SPIO, by correlating the relaxation of the SPIO as a monotonic function of temperature [136]. In another work, Pantke et al. proposed a multi-frequency excitation approach to measure temperature and viscosity of SPIO environment [137]. Combined MPI-MFH systems may soon permit thermal monitoring and dosimetry before, during and after MFH treatment. While measured viscosity changes can be correlated to the degree of ablated tissue death that is brought about after treatment [138].

More recently, newer approaches in combining MFH to modulate drug delivery were explored [92]. This is achieved by a multi-functional nanoparticle design, comprised of SPIOs and a drug of interest, within a polymer matrix with thermo-labile chemical cross-links [139, 140]. The thermally labile bond breaks due to localized heated generated by SPIOs in response to RF excitation, eluting drug in the process. The process of RF actuated drug delivery requires reduced exposure of RF to the subject, thereby greatly reducing the SAR effect, while the controlled drug release improves drug efficacy. Peiris et al, developed a SPIO based nanoparticle chain assembly (shown in Figure 9) that mechanically oscillates when subjected to RF field, shredding the nanocarrier and allowing for controlled release of drug from the chain-assembly [141].

Similar to using an FFR for spatially localizing heat, few researchers have also attempted to spatially control the release of drug using FFR generated with a gradient magnetic field [142, 143]. Fuller et al. developed a thermo-labile drug co-polymer conjugate encapsulating iron oxide nanoparticle, and provided a proof-of-concept spatially controlled drug release using an FFR generated using a 1.27 T/m magnetic field gradient [143]. In another study, iron oxide nanoparticles were co-encapsulated in liposomes (containing the drug of choice), of a low phase transition temperature. Magnetic hyperthermia from RF oscillation resulted in an increase in temperature causing a phase transition in the liposome and selectively triggering drug elution, within a target region of ~3.2 mm radius [142]. Spatially localized heat generation and release of drug, apart from providing combinatorial effect in treating tumors, will also be invaluable for reducing the systemic toxicity of the drug.

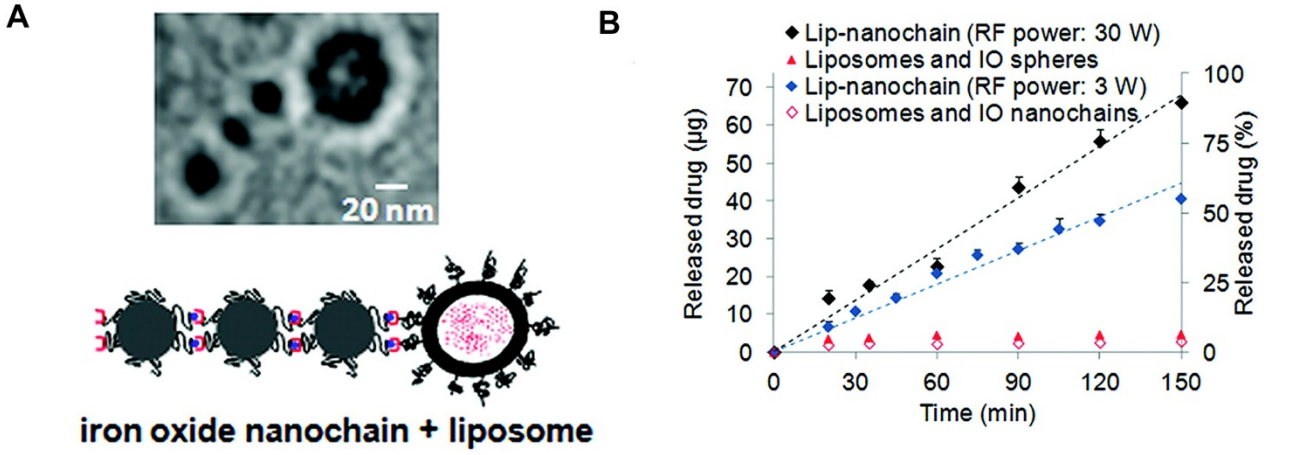

Figure 9: Newer theranostic approaches exploiting SPIO response to RF for controlled drug release. Oscillation from RF fields can be used to actuate drug release from a chained nanoparticle system. (Adapted with permission from [141], ACS Nano (2012). Copyright 2012 American Chemical Society.)

Another theranostic approach is to selectively maneuver SPIOs using gradient magnetic field towards the target tissue. For instance, SPIOs delivered to lungs as inhaled-aerosol can be additionally moved in an image-guided fashion to a target region of the lung (for example a tumor lesion), thus improving therapeutic efficacy [53, 55, 61, 144].

Apart from localized heat deposition and drug delivery, there is a possibility for gradient based localized MFH approach to be extended for neuromodulation through remote excitation of implanted SPIO. The heat generated from the RF excitation of SPIO can trigger genetically modified heat sensitive protein transporter channels in the neurons, that can elicit an action potential [145-147].

MPI in combination with MFH and carefully engineered nanoparticles can provide superb sensitivity and contrast as well as precise actuation of magnetic-based therapies and will be a promising theranostic platform.

Discussion & Conclusion

Image guided treatment techniques have shown effectiveness in improving precision in localizing the treatment. Image guided RF ablation technique and focused ultrasound are currently in development for treating lesions. While RF hyperthermia technique is limited due to the difficulty to focus ($\lambda/2 \sim 50$ m) [73], focused ultrasound can be difficult to be implemented in region such as brain due to sound reflective property of the skull [148].

Magnetic Fluid Hyperthermia (MFH) on the other hand has been in development for many years but has just recently come into increasing clinical use. Moreover, novel innovations are rapidly increasing the efficacy of the technique. MFH is currently FDA approved in the US, with the completion of stage 1 enrollment of 120 patients. A follow up single-arm study has been proposed for focal ablation of solid prostate cancer that will be conducted at University of Texas, San Antonio and University of Seattle, Washington [149].

MPI is a novel and developing imaging modality that has already found complementary usefulness in diagnosing various disease ailments. Currently, only preclinical MPI scanners are available through Bruker GmbH and Magnetic Insight Inc, enabling its use in a vast array of biomedical research. Innovations such a Magnetic Particle Imaging (MPI) can streamline the treatment protocol by complementing MFH through treatment planning including dosimetry, thermometry and post-treatment monitoring of the tumor. MPI now allows for well-localized MFH, removing the concern for non-specific deposition of heat. However, realization of a clinical scanner requires addressing both the regulatory and safety requirements. Scaling up an MPI-MFH system will require higher power and increased cost. MPI-MFH tailored SPIOs with high resolution and sensitivity with efficient heating performance would require rigorous screening for FDA approval [28]. Tissue SAR due to RF excitation needs careful consideration while performing MFH. A cooling blanket around a patient can mitigate heating during MFH procedure. Further, delivering adequate amount of SPIO to tumor non–invasively across various physiological barriers for MFH is challenging, with almost all MFH procedure being carried out with intra-tumoral delivery of nanoparticles. Newer magnetic field gradient based approaches under investigation, can provide improved delivery of SPIO particles to tumor by creating a radial force that can carry the particle across the tumor endothelium [150, 151].

With added benefit of MPI for MFH, FDA approval for MPI can be fast tracked for theranostics through specialized consideration depending on the overall survival benefit of the MPI guided MFH treatment. Clinically translatable prototypes of MPI scanners are currently being designed and reviewed [152, 153]. Further, approaches with tunable field-free region can provide better control and precision in heat deposition. Novel nanoparticle design, can facilitate efficient targeting of tumor required for MFH, and other newer combinatorial approaches can give rise to safer alternatives for treatment of cancer [154-157].

Abbreviations

MPI: Magnetic Particle Imaging; SPIO: Superparamagnetic iron-oxide nanoparticles; CT: Computed Tomography; MRI: Magnetic Resonance Imaging; FFR: field-free-region; HIFU: high-intensity focused ultrasound; US: Ultrasound; FDA: Food and Drug Administration; EU: European Union; FFL: field-free line; FOV: field-of-view; PSF: point-spread-function; SAR: Specific absorption rate; PNS: Peripheral Nerve Stimulation; ILP: Intrinsic loss of parameter; CEM43: cumulative equivalent minutes; RES: reticuloendothelial system; WBC: white blood cells.

Acknowledgements

We gratefully acknowledge support from NIH grants R01 EB019458 and EB024578, UC TRDRP grant 26IP-0049, M. Cook Chair, Bakar Fellowship and the UC Discovery Award.

Competing Interests

Professor Conolly is a co-founder of an MPI startup company, Magnetic Insight, and he holds stock in this company. Dr. Goodwill is CTO of

Magnetic Insight. Drs. Daniel Hens- ley, Elaine Yu and Ryan Orendorff are employees of Magnetic Insight No other competing interests.

References

1. Tay ZW, Chandrasekharan P, Chiu-Lam A, Hensley DW, Dhavalikar R, Zhou XY, et al. Magnetic particle imaging-guided heating in vivo using gradient fields for arbitrary localization of magnetic hyperthermia therapy. ACS Nano. 2018; 12: 3699-713.
2. Yu EY, Bishop M, Zheng B, Ferguson RM, Khandhar AP, Kemp SJ, et al. Magnetic particle imaging: a novel in vivo imaging platform for cancer detection. Nano Lett. 2017; 17: 1648-54.
3. Malietzis G, Monzon L, Hand J, Wasan H, Leen E, Abel M, et al. High-intensity focused ultrasound: advances in technology and experimental trials support enhanced utility of focused ultrasound surgery in oncology. Br J Radiol. 2013; 86: 20130044.
4. Rosnitskiy PB, Yuldashev PV, Sapozhnikov OA, Maxwell AD, Kreider W, Bailey MR, et al. Design of HIFU transducers for generating specified nonlinear ultrasound fields. IEEE Trans Ultrason Ferroelectr Freq Control. 2017; 64: 374-90.
5. Pastis NJ, Greer TJ, Tanner NT, Wahlquist AE, Gordon LL, Sharma AK, et al. Assessing the usefulness of 18F-fluorodeoxyglucose PET-CT scan after stereotactic body radiotherapy for early-stage non-small cell lung cancer. Chest. 2014; 146: 406-11.
6. Li Q, Kim J, Balagurunathan Y, Qi J, Liu Y, Latifi K, et al. CT imaging features associated with recurrence in non-small cell lung cancer patients after stereotactic body radiotherapy. Radiat Oncol. 2017; 12: 158.
7. Pfleiderer SO, Freesmeyer MG, Marx C, Kühne-Heid R, Schneider A, Kaiser WA. Cryotherapy of breast cancer under ultrasound guidance: initial results and limitations. Eur Radiol. 2002; 12: 3009-14.
8. Pfleiderer SOR, Marx C, Camara O, Gajda M, Kaiser WA. Ultrasound-guided, percutaneous cryotherapy of small (≤15 mm) breast cancers. Invest Radiol. 2005; 40: 472-7.
9. Köhler MO, Mougenot C, Quesson B, Enholm J, Le Bail B, Laurent C, et al. Volumetric HIFU ablation under 3D guidance of rapid MRI thermometry. Med Phys. 2009; 36: 3521-35.
10. Kovatcheva RD, Vlahov JD, Stoinov JI, Zaletel K. Benign solid thyroid nodules: US-guided high-intensity focused ultrasound ablation—initial clinical outcomes. Radiology. 2015; 276: 597-605.
11. Piersol GM. Therapeutic Application of Heat: Its Uses and Abuses. N Engl J Med. 1952; 247: 346-9.
12. Gilchrist RK, Medal R, Shorey WD, Hanselman RC, Parrott JC, Taylor CB. Selective inductive heating of lymph nodes. Ann Surg. 1957; 146: 596-606.
13. Pouliquen D, Le Jeune JJ, Perdrisot R, Ermias A, Jallet P. Iron oxide nanoparticles for use as an MRI contrast agent: Pharmacokinetics and metabolism. Magn Reson Imaging. 1991; 9: 275-83.
14. Keselman P, Yu EY, Zhou XY, Goodwill PW, Chandrasekharan P, Ferguson RM, et al. Tracking short-term biodistribution and long-term clearance of SPIO tracers in magnetic particle imaging. Phys Med Biol. 2017; 62: 3440-53.
15. Ruangwattanapaisarn N, Hsiao A, Vasanawala SS. Ferumoxytol as an off-label contrast agent in body 3T MR angiography: a pilot study in children. Pediatr Radiol. 2015; 45: 831-9.
16. Vasanawala SS, Nguyen K-L, Hope MD, Bridges MD, Hope TA, Reeder SB, et al. Safety and technique of ferumoxytol administration for MRI. Magn Reson Med. 2016; 75: 2107-11.
17. Hernando D, Levin YS, Sirlin CB, Reeder SB. Quantification of liver iron with MRI: State of the art and remaining challenges. J Magn Reson Imaging. 2014; 40: 1003-21.
18. Girard OM, Ramirez R, McCarty S, Mattrey RF. Toward absolute quantification of iron oxide nanoparticles as well as cell internalized fraction using multiparametric MRI. Contrast Media Mol Imaging. 2012; 7: 411-7.
19. Gleich B, Weizenecker J. Tomographic imaging using the nonlinear response of magnetic particles. Nature. 2005; 435: 1214-7.
20. Them K, Kaul MG, Jung C, Hofmann M, Mummert T, Werner F, et al. Sensitivity enhancement in magnetic particle imaging by background subtraction. IEEE Trans Med Imaging. 2016; 35: 893-900.
21. Them K, Salamon J, Szwargulski P, Sequeira S, Kaul MG, Lange C, et al. Increasing the sensitivity for stem cell monitoring in system-function based magnetic particle imaging. Phys Med Biol. 2016; 61: 3279-90.
22. Zheng B, von See MP, Yu E, Gunel B, Lu K, Vazin T, et al. Quantitative magnetic particle imaging monitors the transplantation, biodistribution, and clearance of stem cells *in vivo*. Theranostics. 2016; 6: 291-301.
23. Zheng B, Yu E, Orendorff R, Lu K, Konkle JJ, Tay ZW, et al. Seeing SPIOs directly in vivo with magnetic particle imaging. Mol Imaging Biol. 2017; 19: 385-90.
24. Graeser M, Knopp T, Szwargulski P, Friedrich T, von Gladiss A, Kaul M, et al. Towards picogram detection of superparamagnetic iron-oxide particles using a gradiometric receive coil. Sci Rep. 2017; 7: 6872.
25. Ludewig P, Gdaniec N, Sedlacik J, Forkert ND, Szwargulski P, Graeser M, et al. Magnetic particle imaging for real-time perfusion imaging in acute stroke. ACS Nano. 2017; 11: 10480-8.
26. Kuboyabu T, Yamawaki M, Aoki M, Ohki A, Murase K. Quantitative evaluation of tumor early response to magnetic hyperthermia combined with vascular disrupting therapy using magnetic particle imaging. Int J Nanomed Nanosurg. 2016; 2: 1-7.
27. Weissleder R, Stark DD, Engelstad BL, Bacon BR, Compton CC, White DL, et al. Superparamagnetic iron oxide: pharmacokinetics and toxicity. AJR Am J Roentgenol. 1989; 152: 167-73.
28. Lu M, Cohen MH, Rieves D, Pazdur R. FDA report: Ferumoxytol for intravenous iron therapy in adult patients with chronic kidney disease. Am J Hematol. 2010; 85: 315-9.
29. Goodwill PW, Saritas EU, Croft LR, Kim TN, Krishnan KM, Schaffer DV, et al. X-Space MPI: Magnetic nanoparticles for safe medical imaging. Adv Mater. 2012; 24: 3870-7.
30. Zheng B, Vazin T, Goodwill PW, Conway A, Verma A, Ulku Saritas E, et al. Magnetic particle imaging tracks the long-term fate of in vivo neural cell implants with high image contrast. Sci Rep 2015; 5: 14055.
31. Song G, Chen M, Zhang Y, Cui L, Qu H, Zheng X, et al. Janus iron oxides @ semiconducting polymer nanoparticle tracer for cell tracking by magnetic particle imaging. Nano Lett. 2018; 18: 182-9.
32. Saritas EU, Goodwill PW, Croft LR, Konkle JJ, Lu K, Zheng B, et al. Magnetic particle imaging (MPI) for NMR and MRI researchers. J Magn Reson. 2013; 229: 116-26.
33. Goodwill PW, Lu K, Zheng B, Conolly SM. An x-space magnetic particle imaging scanner. Rev Sci Instrum. 2012; 83: 033708.
34. Rahmer J, Halkola A, Gleich B, Schmale I, Borgert J. First experimental evidence of the feasibility of multi-color magnetic particle imaging. Phys Med Biol. 2015; 60: 1775-91.
35. Schulz V, Straub M, Mahlke M, Hubertus S, Lammers T, Kiessling F. A field cancellation signal extraction method for magnetic particle imaging. IEEE Trans Magn. 2015; 51: 1-4.
36. Utkur M, Muslu Y, Saritas EU. Relaxation-based viscosity mapping for magnetic particle imaging. Phys Med Biol. 2017; 62: 3422-39.
37. Murase K, Hiratsuka S, Song R, Takeuchi Y. Development of a system for magnetic particle imaging using neodymium magnets and gradiometer. Jpn J Appl Phys. 2014; 53: 067001.
38. Du Y, Liu X, Liang Q, Liang X-J, Tian J. Optimization and design of magnetic ferrite nanoparticles with uniform tumor distribution for highly sensitive MRI/MPI performance and improved magnetic hyperthermia therapy. Nano Lett. 2019; 19: 3618-26.
39. Bagheri H, Hayden ME. Resolution enhancement in magnetic particle imaging via phase-weighting. J Magn Magn Mater. 2020; 498: 166021.
40. Makela AV, Gaudet JM, Schott MA, Sehl OC, Contag CH, Foster PJ. Magnetic particle imaging of macrophages associated with cancer: Filling the voids left by iron-based magnetic resonance imaging. Mol Imaging Biol. 2020; [Epub ahead of print].
41. Bauer LM, Situ SF, Griswold MA, Samia ACS. High-performance iron oxide nanoparticles for magnetic particle imaging – guided hyperthermia (hMPI). Nanoscale. 2016; 8: 12162-9.
42. Cooley CZ, Mandeville JB, Mason EE, Mandeville ET, Wald LL. Rodent Cerebral Blood Volume (CBV) changes during hypercapnia observed using Magnetic Particle Imaging (MPI) detection. Neuroimage. 2018; 178: 713-20.
43. Nejadnik H, Pandit P, Lenkov O, Lahiji AP, Yerneni K, Daldrup-Link HE. Ferumoxytol can be used for quantitative magnetic particle imaging of transplanted stem cells. Mol Imaging Biol. 2019; 21: 465-72.
44. Wang P, Goodwill PW, Pandit P, Gaudet J, Ross A, Wang J, et al. Magnetic particle imaging of islet transplantation in the liver and under the kidney capsule in mouse models. Quant Imaging Med Surg. 2018; 8: 114-22.
45. Unni M, Uhl AM, Savliwala S, Savitzky BH, Dhavalikar R, Garraud N, et al. Thermal decomposition synthesis of iron oxide nanoparticles with diminished magnetic dead layer by controlled addition of oxygen. ACS Nano. 2017; 11: 2284-303.
46. Zhou XY, Jeffris KE, Yu EY, Zheng B, Goodwill PW, Nahid P, et al. First in vivo magnetic particle imaging of lung perfusion in rats. Phys Med Biol. 2017; 62: 3510-22.
47. Yu EY, Chandrasekharan P, Berzon R, Tay ZW, Zhou XY, Khandhar AP, et al. Magnetic particle imaging for highly sensitive, quantitative, and

safe in vivo gut bleed detection in a murine model. ACS Nano. 2017; 11: 12067-76.
48. Chandrasekharan P, Tay ZW, Zhou XY, Yu E, Orendorff R, Hensley D, et al. A perspective on a rapid and radiation-free tracer imaging modality, magnetic particle imaging, with promise for clinical translation. Br J Radiol. 2018; 91: 20180326.
49. Zhou XY, Tay ZW, Chandrasekharan P, Yu EY, Hensley DW, Orendorff R, et al. Magnetic particle imaging for radiation-free, sensitive and high-contrast vascular imaging and cell tracking. Curr Opin Chem Biol. 2018; 45: 131-8.
50. Salamon J, Hofmann M, Jung C, Kaul MG, Werner F, Them K, et al. Magnetic Particle / Magnetic Resonance Imaging: In-Vitro MPI-Guided Real Time Catheter Tracking and 4D Angioplasty Using a Road Map and Blood Pool Tracer Approach. PLoS One. 2016; 11: e0156899.
51. Rahmer J, Wirtz D, Bontus C, Borgert J, Gleich B. Interactive magnetic catheter steering with 3-d real-time feedback using multi-color magnetic particle imaging. IEEE Trans Med Imaging. 2017; 36: 1449-56.
52. Haegele J, Rahmer J, Gleich B, Borgert J, Wojtczyk H, Panagiotopoulos N, et al. Magnetic particle imaging: visualization of instruments for cardiovascular intervention. Radiology. 2012; 265: 933-8.
53. Banura N, Murase K. Magnetic particle imaging for aerosol-based magnetic targeting. Jpn J Appl Phys. 2017; 56: 088001.
54. Nishimoto K, Mimura A, Aoki M, Banura N, Murase K. Application of magnetic particle imaging to pulmonary imaging using nebulized magnetic nanoparticles. Open J Med Imaging. 2015; 5: 49-55.
55. Tay ZW, Chandrasekharan P, Zhou XY, Yu E, Zheng B, Conolly S. In vivo tracking and quantification of inhaled aerosol using magnetic particle imaging towards inhaled therapeutic monitoring. Theranostics. 2018; 8: 3676-87.
56. Wegner F, Buzug TM, Barkhausen J. Take a deep breath - monitoring of inhaled nanoparticles with magnetic particle imaging. Theranostics. 2018; 8: 3691-2.
57. Zhu X, Li J, Peng P, Hosseini Nassab N, Smith BR. Quantitative drug release monitoring in tumors of living subjects by magnetic particle imaging nanocomposite. Nano Lett. 2019; 19: 6725-33.
58. Fidler F, Steinke M, Kraupner A, Grüttner C, Hiller K, Briel A, et al. Stem cell vitality assessment using magnetic particle spectroscopy. IEEE Trans Magn. 2015; 51: 1-4.
59. Orendorff R, Peck AJ, Zheng B, Shirazi SN, Matthew Ferguson R, Khandhar AP, et al. First in vivo traumatic brain injury imaging via magnetic particle imaging. Phys Med Biol. 2017; 62: 3501-9.
60. Hensley D, Tay ZW, Dhavalikar R, Zheng B, Goodwill P, Rinaldi C, et al. Combining magnetic particle imaging and magnetic fluid hyperthermia in a theranostic platform. Phys Med Biol. 2017; 62: 3483-500.
61. Murase K, Aoki M, Banura N, Nishimoto K, Mimura A, Kuboyabu T, et al. Usefulness of magnetic particle imaging for predicting the therapeutic effect of magnetic hyperthermia. Open J Med Imaging. 2015; 5: 85-99.
62. Murase K, Takata H, Takeuchi Y, Saito S. Control of the temperature rise in magnetic hyperthermia with use of an external static magnetic field. Phys Med. 2013; 29: 624-30.
63. Goodwill PW, Conolly SM. The X-Space formulation of the magnetic particle imaging process: 1-d signal, resolution, bandwidth, snr, sar, and magnetostimulation. IEEE Trans Med Imaging. 2010; 29: 1851-9.
64. Konkle JJ, Goodwill PW, Carrasco-Zevallos OM, Conolly SM. Projection reconstruction magnetic particle imaging. IEEE Trans Med Imaging. 2013; 32: 338-47.
65. Hensley D, Tay ZW, Dhavalikar R, Goodwill P, Zheng B, Rinaldi C, et al. A theranostic platform for localized magnetic fluid hyperthermia and magnetic particle imaging. SPIE BiOS. 2017; 10066-03: 1-8.
66. Dhavalikar R, Rinaldi C. Theoretical predictions for spatially-focused heating of magnetic nanoparticles guided by magnetic particle imaging field gradients. J Magn Magn Mater. 2016; 419: 267-73.
67. IEC. International electrotechnical commission, medical electrical equipment, particular requirements for the safety of magnetic resonance equipment for medical diagnosis. International Standard IEC, Geneva. 2002; 2: 3.
68. US Department of Health and Human Services, Food and Drug Administration, Center for Devices and Radiological Health, Guidance for industry and FDA staff. Criteria for signicant risk investigations of magnetic resonance diagnostic devices. Rockville, MD: US Food and Drug Administration; 2003.
69. Jin J. Electromagnetic analysis and design in magnetic resonance imaging. CRC Press; 1998.
70. Osepchuk JM, Petersen RC. Historical review of RF exposure standards and the International Committee on Electromagnetic Safety (ICES). Bioelectromagnetics. 2003; 24: S7-S16.
71. Saritas EU, Goodwill PW, Zhang GZ, Conolly SM. Magnetostimulation limits in magnetic particle imaging. IEEE Trans Med Imaging. 2013; 32: 1600-10.
72. Irnich W, Schmitt F. Magnetostimulation in MRI. Magn Reson Med. 1995; 33: 619-23.
73. Vorst AV, Rosen A, Kotsuka Y. Fundamentals of electromagnetics. RF/Microwave interaction with biological tissues. Wiley Online Library; 2005.
74. Wildeboer RR, Southern P, Pankhurst QA. On the reliable measurement of specific absorption rates and intrinsic loss parameters in magnetic hyperthermia materials. J Phys D Appl Phys. 2014; 47: 495003.
75. Rosensweig RE. Heating magnetic fluid with alternating magnetic field. J Magn Magn Mater. 2002; 252: 370-4.
76. Hasegawa D, Nakasaka S, Sato M, Ogawa T, Takahashi M. Magnetization process of h.c.p.-CoIr nanoparticles with negative uniaxial magnetocrystalline anisotropy. IEEE Trans Magn. 2006; 42: 2805-7.
77. Eggeman AS, Majetich SA, Farrell D, Pankhurst QA. Size and concentration effects on high frequency hysteresis of iron oxide nanoparticles. IEEE Trans Magn. 2007; 43: 2451-3.
78. Guardia P, Di Corato R, Lartigue L, Wilhelm C, Espinosa A, Garcia-Hernandez M, et al. Water-soluble iron oxide nanocubes with high values of specific absorption rate for cancer cell hyperthermia treatment. ACS Nano. 2012; 6: 3080-91.
79. Xie W, Guo Z, Gao F, Gao Q, Wang D, Liaw BS, et al. Shape-, size- and structure-controlled synthesis and biocompatibility of iron oxide nanoparticles for magnetic theranostics. Theranostics. 2018; 8: 3284-307.
80. Khurshid H, Alonso J, Nemati Z, Phan MH, Mukherjee P, Fdez-Gubieda ML, et al. Anisotropy effects in magnetic hyperthermia: A comparison between spherical and cubic exchange-coupled FeO/Fe3O4 nanoparticles. J Appl Phys. 2015; 117: 17A337.
81. Tong S, Quinto CA, Zhang L, Mohindra P, Bao G. Size-dependent heating of magnetic iron oxide nanoparticles. ACS Nano. 2017; 11: 6808-16.
82. Abenojar EC, Wickramasinghe S, Bas-Concepcion J, Samia ACS. Structural effects on the magnetic hyperthermia properties of iron oxide nanoparticles. Prog Nat Sci-Mater Int. 2016; 26: 440-8.
83. Cabrera D, Camarero J, Ortega D, Teran FJ. Influence of the aggregation, concentration, and viscosity on the nanomagnetism of iron oxide nanoparticle colloids for magnetic hyperthermia. J Nanopart Res. 2015; 17: 121.
84. Engelmann UM, Buhl EM, Draack S, Viereck T, Ludwig F, Schmitz-Rode T, et al. Magnetic relaxation of agglomerated and immobilized iron oxide nanoparticles for hyperthermia and imaging applications. IEEE Magn Lett. 2018; 9: 1-5.
85. Chandrasekharan P, Maity D, Yong CX, Chuang K-H, Ding J, Feng S-S. Vitamin E (d-alpha-tocopheryl-co-poly(ethylene glycol) 1000 succinate) micelles-superparamagnetic iron oxide nanoparticles for enhanced thermotherapy and MRI. Biomaterials. 2011; 32: 5663-72.
86. Hayashi K, Nakamura M, Sakamoto W, Yogo T, Miki H, Ozaki S, et al. Superparamagnetic nanoparticle clusters for cancer theranostics combining magnetic resonance imaging and hyperthermia treatment. Theranostics. 2013; 3: 366-76.
87. Fellows BD, Sandler S, Livingston J, Fuller K, Nwandu L, Timmins S, et al. Extended LaMer synthesis of cobalt-doped ferrite. IEEE Magn Lett. 2018; 9: 1-5.
88. Peng E, Choo ESG, Chandrasekharan P, Yang C-T, Ding J, Chuang K-H, et al. Synthesis of manganese ferrite/graphene oxide nanocomposites for biomedical applications. Small. 2012; 8: 3620-30.
89. Apostolov A, Apostolova I, Wesselinowa J. Specific absorption rate in Zn-doted ferrites for self-controlled magnetic hyperthermia. Eur Phys J B. 2019; 92: 58.
90. Dennis CL, Ivkov R. Physics of heat generation using magnetic nanoparticles for hyperthermia. Int J Hyperthermia. 2013; 29: 715-29.
91. Chantrell R, Popplewell J, Charles S. Measurements of particle size distribution parameters in ferrofluids. IEEE Trans Magn. 1978; 14: 975-7.
92. Kumar CSSR, Mohammad F. Magnetic nanomaterials for hyperthermia-based therapy and controlled drug delivery. Adv Drug Deliv Rev. 2011; 63: 789-808.
93. Jordan A, Scholz R, Wust P, Schirra H, Thomas S, Schmidt H, et al. Endocytosis of dextran and silan-coated magnetite nanoparticles and the effect of intracellular hyperthermia on human mammary carcinoma cells in vitro. J Magn Magn Mater. 1999; 194: 185-96.
94. Liu XL, Fan HM, Yi JB, Yang Y, Choo ESG, Xue JM, et al. Optimization of surface coating on Fe3O4 nanoparticles for high performance magnetic hyperthermia agents. J Mater Chem. 2012; 22: 8235-44.
95. Tay ZW, Hensley DW, Vreeland EC, Zheng B, Conolly SM. The relaxation wall: experimental limits to improving MPI spatial resolution by increasing nanoparticle core size. Biomed Phys Eng Express. 2017; 3: 035003.
96. Tay ZW, Hensley DW, Chandrasekharan P, Zheng B, Conolly SM. Optimization of drive parameters for resolution, sensitivity and safety in

magnetic particle imaging. IEEE Trans Med Imaging. 2019; [Epub ahead of print].
97. Lu K, Goodwill PW, Saritas EU, Zheng B, Conolly SM. Linearity and shift invariance for quantitative magnetic particle imaging. IEEE Trans Med Imaging. 2013; 32: 1565-75.
98. Tay ZW, Hensley D, Ma J, Chandrasekharan P, Zheng B, Goodwill P, et al. Pulsed excitation in magnetic particle imaging. IEEE Trans Med Imaging. 2019; 38: 2389-99.
99. Liu Y, Fan H, Guo Q, Jiang A, Du X, Zhou J. Ultra-small pH-responsive Nd-doped NaDyF4 Nanoagents for Enhanced Cancer Theranostic by in situ Aggregation. Theranostics. 2017; 7: 4217-28.
100. Wilhelm S, Tavares AJ, Dai Q, Ohta S, Audet J, Dvorak HF, et al. Analysis of nanoparticle delivery to tumours. Nat Rev Mater. 2016; 1: 16014.
101. Maity D, Chandrasekharan P, Feng S, Jun D. Synthesis and studies of APTES functionalized magnetite nanoparticles. 2010 International Conference on Nanoscience and Nanotechnology; 2010. p. 94-7.
102. Maity D, Chandrasekharan P, Pradhan P, Chuang K-H, Xue J-M, Feng S-S, et al. Novel synthesis of superparamagnetic magnetite nanoclusters for biomedical applications. J Mater Chem. 2011; 21: 14717-24.
103. Youhannayee M, Nakhaei-Rad S, Haghighi F, Klauke K, Janiak C, Ahmadian MR, et al. Physical characterization and uptake of iron oxide nanoparticles of different prostate cancer cells. J Magn Magn Mater. 2019; 473: 205-14.
104. Jordan A, Scholz R, Wust P, Fähling H, Felix R. Magnetic fluid hyperthermia (MFH): Cancer treatment with AC magnetic field induced excitation of biocompatible superparamagnetic nanoparticles. J Magn Magn Mater. 1999; 201: 413-9.
105. Andrä W, Nowak H. Magnetism in Medicine: A Handbook. 2 ed: Wiley Online Library; 2006.
106. Chang D, Lim M, Goos JACM, Qiao R, Ng YY, Mansfeld FM, et al. Biologically targeted magnetic hyperthermia: potential and limitations. Front Pharmacol. 2018; 9: 831.
107. Multhoff G, Botzler C, Jennen L, Schmidt J, Ellwart J, Issels R. Heat shock protein 72 on tumor cells: a recognition structure for natural killer cells. J Immunol. 1997; 158: 4341-50.
108. Calderwood SK, Theriault JR, Gong J. How is the immune response affected by hyperthermia and heat shock proteins? Int J Hyperthermia. 2005; 21: 713-6.
109. Song CW. Effect of local hyperthermia on blood flow and microenvironment: A review. Cancer Res. 1984; 44: 4721s-30s.
110. Creixell M, Bohórquez AC, Torres-Lugo M, Rinaldi C. EGFR-Targeted magnetic nanoparticle heaters kill cancer cells without a perceptible temperature rise. ACS Nano. 2011; 5: 7124-9.
111. Raval YS, Fellows BD, Murbach J, Cordeau Y, Mefford OT, Tzeng T-RJ. Multianchored glycoconjugate-functionalized magnetic nanoparticles: a tool for selective killing of targeted bacteria via alternating magnetic fields. Adv Funct Mater. 2017; 27: 1701473.
112. Sapareto SA, Dewey WC. Thermal dose determination in cancer therapy. Int J Radiat Oncol Biol Phys. 1984; 10: 787-800.
113. van Rhoon GC, Samaras T, Yarmolenko PS, Dewhirst MW, Neufeld E, Kuster N. CEM43 degrees C thermal dose thresholds: a potential guide for magnetic resonance radiofrequency exposure levels? Eur Radiol. 2013; 23: 2215-27.
114. Hall EJ, Roizin-Towle L. Biological Effects of Heat. Cancer Res. 1984; 44: 4708s-13s.
115. Mizzen LA, Welch WJ. Characterization of the thermotolerant cell. I. Effects on protein synthesis activity and the regulation of heat-shock protein 70 expression. J Cell Biol. 1988; 106: 1105-16.
116. Welch WJ, Mizzen LA. Characterization of the thermotolerant cell. II. Effects on the intracellular distribution of heat-shock protein 70, intermediate filaments, and small nuclear ribonucleoprotein complexes. J Cell Biol. 1988; 106: 1117-30.
117. Moseley PL. Heat shock proteins and heat adaptation of the whole organism. J Appl Physiol. 1997; 83: 1413-7.
118. Dewey WC. Arrhenius relationships from the molecule and cell to the clinic. Int J Hyperthermia. 2009; 25: 3-20.
119. Maier-Hauff K, Ulrich F, Nestler D, Niehoff H, Wust P, Thiesen B, et al. Efficacy and safety of intratumoral thermotherapy using magnetic iron-oxide nanoparticles combined with external beam radiotherapy on patients with recurrent glioblastoma multiforme. J Neurooncol. 2011; 103: 317-24.
120. Johannsen M, Gneveckow U, Eckelt L, Feussner A, Waldofner N, Scholz R, et al. Clinical hyperthermia of prostate cancer using magnetic nanoparticles: presentation of a new interstitial technique. Int J Hyperthermia. 2005; 21: 637-47.
121. Li B, Wang X, Chen L, Zhou Y, Dang W, Chang J, et al. Ultrathin Cu-TCPP MOF nanosheets: a new theragnostic nanoplatform with magnetic resonance/near-infrared thermal imaging for synergistic phototherapy of cancers. Theranostics. 2018; 8: 4086-96.
122. Gneveckow U, Jordan A, Scholz R, Brüß V, Waldöfner N, Ricke J, et al. Description and characterization of the novel hyperthermia- and thermoablation-system for clinical magnetic fluid hyperthermia. Med Phys. 2004; 31: 1444-51.
123. Jordan A, Scholz R, Maier-Hauff K, Johannsen M, Wust P, Nadobny J, et al. Presentation of a new magnetic field therapy system for the treatment of human solid tumors with magnetic fluid hyperthermia. J Magn Magn Mater. 2001; 225: 118-26.
124. Schenck JF. Safety of Strong, Static Magnetic Fields. J Magn Reson Imaging. 2000; 12: 2-19.
125. Rahmer J, Weizenecker J, Gleich B, Borgert J. Signal encoding in magnetic particle imaging: properties of the system function. BMC Med Imaging. 2009; 9: 4.
126. Sebastian AR, Ryu SH, Ko HM, Kim SH. Design and control of field-free region using two permanent magnets for selective magnetic hyperthermia. IEEE Access. 2019; 7: 96094-104.
127. Turner R, Streicher M. Measuring temperature using MRI: a powerful and versatile technique. Magma. 2012; 25: 1-3.
128. Siedek F, Yeo SY, Heijman E, Grinstein O, Bratke G, Heneweer C, et al. Magnetic resonance-guided high-intensity focused ultrasound (MR-HIFU): technical background and overview of current clinical applications (part 1). Rofo. 2019; 191: 522-30.
129. Wyatt C, Soher B, Maccarini P, Charles HC, Stauffer P, Macfall J. Hyperthermia MRI temperature measurement: evaluation of measurement stabilisation strategies for extremity and breast tumours. Int J Hyperthermia. 2009; 25: 422-33.
130. Copelan A, Hartman J, Chehab M, Venkatesan AM. High-intensity focused ultrasound: Current status for image-guided therapy. Semin Intervent Radiol. 2015; 32: 398-415.
131. Goodwill PW, Tamrazian A, Croft LR, Lu CD, Johnson EM, Pidaparthi R, et al. Ferrohydrodynamic relaxometry for magnetic particle imaging. Appl Phys Lett. 2011; 98: 262502.
132. Croft LR, Goodwill PW, Conolly SM. Relaxation in X-Space magnetic particle imaging. IEEE Trans Med Imaging. 2012; 31: 2335-42.
133. Deissler RJ, Wu Y, Martens MA. Dependence of Brownian and Néel relaxation times on magnetic field strength. Med Phys. 2014; 41: 012301.
134. Muslu Y, Utkur M, Demirel OB, Saritas EU. Calibration-free relaxation-based multi-color magnetic particle imaging. IEEE Trans Med Imaging. 2018; 37: 1920-31.
135. Gandhi S, Arami H, Krishnan KM. Detection of cancer-specific proteases using magnetic relaxation of peptide-conjugated nanoparticles in biological environment. Nano Lett. 2016; 16: 3668-74.
136. Weaver JB, Rauwerdink AM, Hansen EW. Magnetic nanoparticle temperature estimation. Med Phys. 2009; 36: 1822-9.
137. Pantke D, Holle N, Mogarkar A, Straub M, Schulz V. Multifrequency magnetic particle imaging enabled by a combined passive and active drive field feed-through compensation approach. Med Phys. 2019; 46: 4077-86.
138. [Internet], Adigun R, Basit H, Murray J. Necrosis, Cell (liquefactive, coagulative, caseous, fat, fibrinoid, and gangrenous). In: StatPearls [Internet] Treasure Island (FL): StatPearls Publishing. 2019 Jan: Available from: https://www.ncbi.nlm.nih.gov/books/NBK430935/.
139. McGill SL, Cuylear CL, Adolphi NL, Osinski M, Smyth HDC. Magnetically responsive nanoparticles for drug delivery applications using low magnetic field strengths. IEEE Trans Nanobioscience. 2009; 8: 33-42.
140. Derfus AM, von Maltzahn G, Harris TJ, Duza T, Vecchio KS, Ruoslahti E, et al. Remotely triggered release from magnetic nanoparticles. Adv Mater. 2007; 19: 3932-6.
141. Peiris PM, Bauer L, Toy R, Tran E, Pansky J, Doolittle E, et al. Enhanced delivery of chemotherapy to tumors using a multicomponent nanochain with radio-frequency-tunable drug release. ACS Nano. 2012; 6: 4157-68.
142. Liu JF, Neel N, Dang P, Lamb M, McKenna J, Rodgers L, et al. Radiofrequency-triggered drug release from nanoliposomes with millimeter-scale resolution using a superimposed static gating field. Small. 2018; 14: 1802563.
143. Fuller EG, Sun H, Dhavalikar RD, Unni M, Scheutz GM, Sumerlin BS, et al. Externally triggered heat and drug release from magnetically controlled nanocarriers. ACS Appl Polym Mater. 2019; 1: 211-20.
144. Kuboyabu T, Ohki A, Banura N, Murase K. Usefulness of magnetic particle imaging for monitoring the effect of magnetic targeting. Open J Med Imaging. 2016; 6: 33-41.
145. Huang H, Delikanli S, Zeng H, Ferkey DM, Pralle A. Remote control of ion channels and neurons through magnetic-field heating of nanoparticles. Nat Nanotechnol. 2010; 5: 602-6.

146. Stanley SA, Gagner JE, Damanpour S, Yoshida M, Dordick JS, Friedman JM. Radio-wave heating of iron oxide nanoparticles can regulate plasma glucose in mice. Science. 2012; 336: 604-8.
147. Chen R, Romero G, Christiansen MG, Mohr A, Anikeeva P. Wireless magnetothermal deep brain stimulation. Science. 2015; 347: 1477-80.
148. Pinton G, Aubry J-F, Bossy E, Muller M, Pernot M, Tanter M. Attenuation, scattering, and absorption of ultrasound in the skull bone. Med Phys. 2012; 39: 299-307.
149. [Internet] Magforce: MagForce AG: MagForce USA I. Completed enrollment and treatment for stage 1 and prepares for next stage of its pivotal, single-arm study for the focal ablation of intermediate risk prostate cancer with nanotherm therapy. 2019. <https://wwwmagforcecom/en/news/?article=308>
150. Liu JF, Lan Z, Ferrari C, Stein JM, Higbee-Dempsey E, Yan L, et al. Use of oppositely polarized external magnets to improve the accumulation and penetration of magnetic nanocarriers into solid tumors. ACS Nano. 2019; [Epub ahead of print].
151. Zhou Z, Shen Z, Chen X. Tale of two magnets: an advanced magnetic targeting system. ACS Nano. 2019; [Epub ahead of print].
152. Graeser M, Thieben F, Szwargulski P, Werner F, Gdaniec N, Boberg M, et al. Human-sized magnetic particle imaging for brain applications. Nat Commun. 2019; 10: 1936.
153. Mason EE, Cooley CZ, Cauley SF, Griswold MA, Conolly SM, Wald LL. Design analysis of an MPI human functional brain scanner. Int J Magn Part Imaging. 2017; 3: 1703008.
154. Curcio A, Silva AKA, Cabana S, Espinosa A, Baptiste B, Menguy N, et al. Iron Oxide Nanoflowers @ CuS Hybrids for Cancer Tri-Therapy: Interplay of Photothermal Therapy, Magnetic Hyperthermia and Photodynamic Therapy. Theranostics. 2019; 9: 1288-302.
155. Hayashi K, Nakamura M, Miki H, Ozaki S, Abe M, Matsumoto T, et al. Magnetically responsive smart nanoparticles for cancer treatment with a combination of magnetic hyperthermia and remote-control drug release. Theranostics. 2014; 4: 834-44.
156. Liu D, Hong Y, Li Y, Hu C, Yip TC, Yu WK, et al. Targeted destruction of cancer stem cells using multifunctional magnetic nanoparticles that enable combined hyperthermia and chemotherapy. Theranostics. 2020; 10: 1181-96.
157. Zhou Y, Han G, Wang Y, Hu X, Li Z, Chen L, et al. Radiofrequency heat-enhanced chemotherapy for breast cancer: towards interventional molecular image-guided chemotherapy. Theranostics. 2014; 4: 1145-52.